

The Effects of oil-in-Water Nanoemulsion Polyethylene Glycol Surface Density on Intracellular Stability, Pharmacokinetics, and Biodistribution in Tumor Bearing Mice

Sjoerd Hak · Zuzana Garaiova · Linda Therese Olsen · Asbjørn Magne Nilsen · Catharina de Lange Davies

Received: 7 July 2014 / Accepted: 10 October 2014 / Published online: 28 October 2014
© Springer Science+Business Media New York 2014

ABSTRACT

Purpose Lipid-based nanoparticles are extensively studied for drug delivery. These nanoparticles are often surface-coated with polyethylene glycol (PEG) to improve their biodistribution. Until now, the effects of varying PEG surface density have been studied in a narrow and low range. Here, the effects of high and a broad range of PEG surface densities on the *in vivo* performance of lipid-based nanoparticles were studied.

Methods Oil-in-water nanoemulsions were prepared with PEG surface densities of 5–50 mol%. Confocal microscopy was used to assess intracellular disintegration *in vitro*. *In vivo* pharmacokinetics and biodistribution in tumor bearing mice were studied using a small animal optical imager.

Results PEG surface density did not affect intracellular nanoemulsion stability. Surprisingly, circulation half-lives decreased with increasing PEG surface density. A plausible explanation was that nanoemulsion with high (50 mol%) PEG surface density activated the complement in a whole blood assay, whereas nanoemulsion with low (5 mol%) PEG density did not. *In vivo*, nanoemulsion with low PEG surface density was mostly confined to the tumor and organs of the mononuclear phagocyte system, whereas nanoemulsion with high PEG density accumulated throughout the mouse.

Conclusions Optimal PEG surface density of lipid-based nanoparticles for tumor targeting was found to be below 10 mol%.

KEY WORDS biodistribution · circulation time · immunotoxicity · lipid-based nanoparticles · PEG

ABBREVIATIONS

ICA	Intensity correlation analysis
ICQ	Intensity correlation quotient
NE	Nanoemulsion
PDM	Product of differences from the mean
PEG	Polyethylene glycol
PEG-DSPE	1,2-distearoyl-sn-glycerol-3-phosphoethanolamine-N-[methoxy(polyethylene-glycol)-2000]
PX (with X = 5, 10, 30, 50)	Nanoemulsion containing X mol% PEG-DSPE
SBR	Signal to background ratio
TCC	Total complement complex

Electronic supplementary material The online version of this article (doi:10.1007/s11095-014-1553-6) contains supplementary material, which is available to authorized users.

S. Hak
MI Lab and Department of Circulation and Medical Imaging, The Norwegian University of Science and Technology, Trondheim, Norway

Z. Garaiova
Department of Nuclear Physics and Biophysics, Faculty of Mathematics, Physics and Informatics, Comenius University, Bratislava, Slovak Republic

L. T. Olsen · A. M. Nilsen
Department of Cancer Research and Molecular Medicine, Faculty of Medicine, The Norwegian University of Science and Technology Trondheim, Norway

C. de Lange Davies
Department of Physics, The Norwegian University of Science and Technology, Trondheim, Norway

S. Hak (✉)
MI Lab MR-senteret, MTFS 3. etg S, NTNU Olav Kyrres gate 9
7030 Trondheim, Norway
e-mail: sjoerd.hak@ntnu.no

INTRODUCTION

In the field of nanomedicine, utilization of nanoparticles as intravenously administered drug delivery systems has become an established approach. Although nanotherapies are being developed for the treatment of a variety of pathologies, like atherosclerosis [1] and arthritis [2], cancer treatment has received the most attention so far. Solid tumors are characterized by an angiogenic, disorganized neovasculature which is highly permeable [3,4]. This enhanced vascular permeability results in the extravasation of nanoparticles into the tumor interstitium. Combined with the often poor lymphatic drainage from solid tumors, this leads to high accumulation of intravenously injected nanoparticles in the tumor tissue. This phenomenon has been called the enhanced permeability and retention (EPR) effect [5,6], and is the key mechanism by which today's clinically approved nanomedicines deliver drugs [7].

One of the most widely studied class of nanoparticles for drug delivery are self-assembled lipid-based nanoparticles. Well-known examples are liposomes, of which multiple formulations have been clinically approved [8], and nanoemulsions which are being intensively investigated [9,10]. Moreover, lipid coating of hydrophobic cores has evolved into a powerful strategy to solubilize, stabilize, and introduce functionality and biocompatibility to a variety of polymer and inorganic nanoparticles, like poly(lactic-co-glycolic acid) (PLGA) [11], iron oxides [12] or qdots [13].

To obtain sufficient levels of nanoparticles in tumors upon intravenous injection, limited recognition by the mononuclear phagocyte system and sufficiently long circulation times are prerequisites. A common approach to achieve both is to coat the nanoparticle surface with polyethylene glycol (PEG) [14–17]. In the majority of lipidic nanoparticles this is achieved through the incorporation of PEG conjugated lipids, or PEG-lipids. PEG is very hydrophilic, is not toxic, has a low level of protein or cellular adsorption, and numerous PEGylated therapeutics have now been FDA-approved [8,15,17]. PEGylation of self-assembled lipid-based nanoparticles provides improved colloidal stability through steric stabilization [14,18], decreases non-specific cellular uptake [19], and typically increases circulation half-lives [14,20]. Additionally, the vascular permeability for PEGylated as compared to non-PEGylated liposomes was found significantly increased, resulting in an improved utilization of the EPR effect [16,21].

One parameter which highly influences the effect PEG surface coatings have on nanoparticle characteristics and behavior is the PEG coating density. The self-assembled nature of lipidic nanoparticles provides high control over this surface density, which has been found to modulate circulation times [18,22,23], non-specific cellular uptake [19], and ligand-targeting efficiency [24]. Most of the available knowledge of effects that PEG surface densities have on the behavior of

lipid-based nanoparticles has been obtained by studying liposomes. The maximum achievable PEG surface density for liposomes without affecting their morphology (obtaining much smaller micellar aggregates instead of liposomes) is below 10% [25]. However, in nanoemulsions and the emerging lipid-coated nanoparticles, achievable PEG surface densities are much higher. Therefore, we investigated the effect of a wide range of PEG surface densities on several critical properties of drug delivery systems utilizing a recently introduced nanoemulsion (NE) platform [24,26]. The unique features of this platform allow increasing the PEG surface density up to 50 mol% without significantly affecting size and size distribution. This makes it possible to study the influence of PEGylation on nanoparticle behavior in a much wider range of PEG surface densities. In a previous study, this platform was successfully used to demonstrate that increasing PEG surface density reduces ligand targeting efficiency both *in vitro* and *in vivo* [24]. In the current study we synthesized NEs with 5, 10, 30, and 50 mol% PEG surface density and studied several important aspects of NE behavior such as *in vitro* cellular uptake and intracellular stability in tumor cells, toxicity in cell cultures and human whole blood, *in vivo* circulation half-lives, and biodistribution and passive tumor targeting in tumor bearing mice.

MATERIAL AND METHODS

Preparation of Nanoemulsions

NEs with 5, 10, 30, and 50% surface PEG density (referred to as P5, P10, P30, and P50, respectively) were prepared using a method based on swift evaporation of organic solvents as previously described [26]. 1,2-distearoyl-sn-glycero-3-phosphocholine (DSPC), cholesterol, and 1,2-distearoyl-sn-glycerol-3-phosphoethanolamine-N-[methoxy(polyethylene glycol)-2000] (PEG-DSPE) (all from Avanti Polar Lipids) were used at molar ratios as denoted in Table I. The amount of soybean oil was defined as mg per μ mole of amphiphilic lipid mixture (Table I). For fluorescence 0.1 mol% of NIR664-PEG²⁰⁰⁰-DSPE (NIR664-PEG-DSPE, SyMo-Chem) and/or 1,2-dipalmitoyl-sn-glycero-3-phosphoethanolamine-N-lissamine rhodamine B sulfonyl ammonium salt (rhodamine-PE; Avanti Polar Lipids), or 1,1'-

Table I Composition of the Different Nanoemulsions

	P5	P10	P30	P50
DSPC (mol%)	62	57	37	17
Cholesterol (mol%)	33	33	33	33
PEG2000-DSPE (mol%)	5	10	30	50
Soybean oil (mg/ μ mol amphiphilic lipid)	2.7	3.2	4	5.4

Diocetadecyl-3,3,3',3'-Tetramethylindotricarbocyanine Iodide (DiR, Invitrogen) were incorporated. All components were mixed in chloroform and added to 3 ml heated sterile filtered HBS buffer (75°C, pH 7.4) under vigorous magnetic stirring (1,100 rpm) in order to evaporate chloroform. The obtained crude emulsion was then sonicated for 20 min (Heat System Ultrasonics, W-225R, duty cycle 35%, 30 W and 20 kHz) at ambient temperature. After this, the NEs were stored in the dark at 4°C until use. From previous work, we know the zeta potential of the NEs to be below -30 mV for all formulations and to become more negative with increasing PEG-DSPE content, see [24].

The particle concentrations used in this study were all given in amphiphilic lipid concentrations as that is the most reported concentration of liposomes and emulsions found in the literature, and it relates linearly to the fluorophore and PEG concentrations.

Dynamic Light Scattering

The hydrodynamic diameter and size distribution of the NEs were measured by dynamic light scattering (DLS) using a Zetasizer Nano (Malvern, UK) following a protocol described previously [24]. Briefly, for size measurements 8 μ L of NE suspension was dispersed in 800 μ L of 200 nm filtered hepes buffered saline in an ordinary cuvette.

Protein Adsorption on Nanoemulsions

The NE (P5, P30, and P50, $n=3$ for each) was mixed in PBS containing 10% fetal bovine serum (FBS) and incubated at 37°C under gentle shaking. The size of the NEs was measured before incubation and after 1 and 24 h using DLS. The results are represented as change in size as compared to the control experiment which was performed in the exact same manner as described above, but in pure PBS without FBS.

Cell Culturing

The human PC3 prostate cancer cell line was grown in monolayers in the presence of Dulbecco's modified eagle growth medium (DMEM, Gibco/Invitrogen) supplemented with 10% FBS at 37°C and 5% CO₂.

Cellular Uptake of Nanoemulsions

Cellular uptake of NEs was measured by flow cytometry (Gallios, Beckman Coulter). 120,000 PC3 cells/well were seeded in 12-well plates (Corning) in 800 μ L of DMEM. After 24 h, DMEM was removed and cells were incubated at 37°C and 5% CO₂ for 2 and 4 h with 400 μ L of either DMEM with NE (1 mM amphiphilic lipid) or as a control only DMEM.

After incubation, the cells were washed 3 times with PBS (1 ml), trypsinized (300 μ L), resuspended in ice cold PBS supplemented with 10% FBS (700 μ L) and kept on ice until flow cytometry analysis. NIR664 was excited at 633 nm and fluorescence was detected at 650–670 nm. For each sample, 10,000 cells were counted. The dead cells, debris and aggregates were excluded by gating the fluorescence on a dot plot of the forward light scatter signal against the side scatter signal. The cellular uptake was measured both as percentage of cells with higher fluorescence intensity than cellular autofluorescence as well as the level of internalized NE, which was obtained from the median fluorescence intensity divided by median autofluorescence and normalized to the observed maximum cellular uptake. Cellular uptake was measured in independent experiments ($n=3$ for P5, P10, P30 and $n=2$ for P50) with 2–3 samples per incubation condition in each experiment.

Intracellular Nanoemulsion Integrity

To study intracellular integrity of the NEs and the effect of PEG surface density on this integrity, PC3 cells were incubated with double labeled (with both rhodamine-PE and NIR664-PEG-DSPE) P5 and P30. Colocalization of the two fluorophores was assessed using confocal laser scanning microscopy (CLSM, Zeiss LSM 510 Meta, Carl Zeiss Jena GmbH). 25,000 cells/well in 300 μ L were seeded on Lab-Tek 8-well detachable chamber slides (VWR International). After 24 h, DMEM was removed and cells were incubated with 200 μ L DMEM containing NE (1 mM amphiphilic lipid) for 2 h. After incubation, NEs were removed and the cells were washed 3 times with 400 μ L DMEM. The cells were subsequently fixed on ice with 400 μ L 4% paraformaldehyde in PBS to avoid movement artefacts in the microscopy. After 30 min, the paraformaldehyde was removed and the cells were washed 2 times with 400 μ L PBS. The samples were mounted with Vectashield antifading reagent (Vector Lab), and the cover glasses were sealed with nail polish. 8-bit, 2 channel z-stack images (652×652 pixels of 0.110×0.110 μ m) were obtained with a Plan Apochromat 63x/1.4 oil immersion objective. Rhodamine-PE was excited at 543 nm and detected at 569–623 nm. NIR664-PEG-DSPE was excited at 633 nm and detected at 655–719 nm. The thickness of each optical slice was ~ 0.9 μ m and the interval between slices ~ 0.45 μ m. Detector gain and laser powers were optimized to record the full range of pixel intensities with a minimum of under and over exposure. To visualize the whole cells, they were imaged using differential interference contrast.

Quantitative Colocalization

Quantitative analysis of colocalization between rhodamine-PE and NIR664-PEG-DSPE in three-dimensional z-stacks was performed in ImageJ (NIH) using the plug-in Intensity

Correlation Analysis (Tony Collins, University Health Network Research, Toronto, Canada). After background subtraction, single cells were manually segmented using differential interference contrast images, thus only the fluorescence from internalized NEs was taken into account. Scatter plots, Pearson's correlation coefficient (R_r), Manders' colocalization coefficients (M), intensity correlation analysis (ICA) plots, and the intensity correlation quotient (ICQ) were determined. For convenience we refer to channel A in case of the NIR664-PEG-DSPE and to channel B in case of the rhodamine-PE.

In a scatter plot, the pixel intensities of the two channels are plotted against each other and distributions along a straight line indicate perfect colocalization. The R_r determines the spread of the distribution around this line by estimating the goodness of a linear approximation and ranges from -1 (perfect negative correlation) to 1 (perfect positive correlation). Hence, the R_r reports covariance and is independent of signal offset (background), but sensitive to noise and variation in fluorescence intensities throughout the image. In practice, values below 0.5 are difficult to interpret [27].

Manders coefficients provide the ratio of the signal in one channel colocalizing with signal in the other channel and range from 0 to 1 . As such M_B describes the fraction of rhodamine signal colocalizing with NIR664 fluorescence and M_A the fraction of NIR664 signal colocalizing with rhodamine fluorescence. Manders coefficients are independent of signal intensity, but they are affected by signal offset (background) and noise.

ICA results are presented in two ICA plots, where the voxel intensities in the two channels are plotted along the Y-axis as a function of the product of differences from the mean (PDM) values along the X-axis. PDM is defined as $(A-a)(B-b)$, where A and a are the voxel intensity and mean intensity in channel A and B and b the voxel intensity and mean intensity in channel B. Colocalized voxels have a positive PDM value and are found on the right side of the Y-axis, whereas segregated voxels have a negative PDM value and are found on the left side of Y-axis. More quantitative information than ICA plots possess is provided by the ICQ. This parameter reflects the degree of dependency between the two channels, not necessarily implying a large number of colocalized voxels, but rather a high covariance. ICQ is defined as the ratio between the number of voxel pairs with positive PDM and the total number of voxel pairs subtracted by 0.5 . As such the ICQ ranges from -0.5 to 0.5 and the values -0.5 , 0 , 0.5 indicate complete segregation, random staining, or dependent staining, respectively.

Cell Viability Assay

Cell viability was assessed using Alamar Blue assay (Invitrogen, DAL1025). In this assay cells are incubated with non-fluorescent resazurin, which is metabolized to fluorescent resorufin by viable cells. PC3 cells were seeded in 96-well

plates (Corning, black bottom) at $10,000$ cells/well in DMEM. After 24 h, the cells were incubated for 2 h with DMEM containing NEs at 0.1 mM, 0.3 mM, 0.5 mM, 1 mM, and 1.5 mM amphiphilic lipid and then washed with phenol red free DMEM, containing penicillin. Subsequently, the cells were incubated with resazurin (10 μ L into 100 μ L of DMEM) for 2 h, and resorufin fluorescence was measured in a microplate fluorometer with excitation at 530 nm and detection at 590 nm. The assay was performed two times with four samples for each condition.

Human Blood Monocyte and Whole Blood Assay

Cytokine production and activation of complement by P5 and P50 was assessed in human blood monocytes and whole blood. Peripheral blood mononuclear cells were prepared from A+ buffy coats given by healthy donors at the blood bank of St. Olavs University Hospital (Trondheim, Norway), by density gradient centrifugation with Lymphoprep (Axis-Shield) based on a method by Bøyum [28]. Monocytes were isolated from the other mononuclear cells by adhesion for 90 min in 96 well culture plates (4×10^6 cells/ml in RPMI 1640 medium with Gentamicine, L-Glutamine and 5% A+ human serum, referred to as complete medium). After washing 3 times with Hank's balanced salt solution (HBSS) the cells were primed with 100 pg/ml lipopolysaccharide in complete medium for 4 h before exposure for 4 h to P5 or P50 in concentrations 1.04×10^{-5} – 10.04 mM (amphiphilic lipid) in dilutions steps of $1:10$. Concentrations of IL- 1β and TNF α were assessed by ELISA and 17 different cytokines (IL- 1β , IL- 2 , IL- 4 , IL- 5 , IL- 6 , IL- 7 , IL- 8 , IL- 10 , IL- 12 , IL- 13 , IL- 17 , G-CSF, GM-CSF, IFN- γ , MCP- 1 , MIP- 1β , TNF- α) were assessed by multiplex (Bio-Rad, Bio-Plex Pro, M50-00031YV) in two different experiment series, respectively, with three donors in each series.

The whole blood assay was performed according to Mollnes *et al.* [29] with blood from four human donors. 500 μ L whole blood with anticoagulant Lepirudin was exposed to 1.04 mM (amphiphilic lipid) P5 or P50 for 0 , 15 , 30 , 60 , 120 or 360 min for analysis of complement receptor 3 (CD11b) expression by granulocytes with flow cytometry (0 , 15 and 60 min), total complement complex (TCC) with ELISA (0 , 30 and 120 min) and 17 different cytokines with multiplex (360 min) (Bio-Rad, Bio-Plex Pro, M50-00031YV). Complement activation was assessed by analysis of CD11b and TCC. Positive controls were zymosan, lipopolysaccharide, ATP and Leu-Leu-OMe and the negative control was sterile PBS. Monocytes were differentiated from granulocytes by the presence of CD14 assessed by binding of anti CD14 fluorescent antibody and flow cytometry.

Approval no. 2009/2245 was received from the Regional Committee for Medical and Health Research Ethics in Central Norway (REC Central), The Norwegian Ministry of

Education and Research, to perform the human whole blood and monocyte experiments. Written informed consent was obtained from all participants.

Animals

The animals used in this study were male athymic Balb/c Nu/nu mice of approximately 20 g. They were kept under pathogen-free conditions at a temperature of 19–22°C, 50–60% humidity, and 65 air changes per h and were allowed food and water *ad libitum*. The experiments were approved by the local ethical committee and adhered to the “Principles of Laboratory Animal Care”.

Circulation Times

The circulation half-lives of the NEs were determined using a previously published protocol [26]. In short, mice were injected with DiR labeled P5, P10, P30, and P50 NE ($n=3$ for all) at an amphiphilic lipid dose of 80 $\mu\text{mole/kg}$. Blood samples were collected from the saphenous vein before and at 5, 15, 30, 60 min and 2, 4, 6, and 24 h post-injection. DiR fluorescence intensity in serum was measured using an optical imager (Pearl Impulse, Licor) and normalized to the weight of the blood sample taken. The obtained fluorescence intensity *versus* time curves were most accurately fitted by mono-exponentials, from which the circulation half-lives were obtained.

Biodistribution

The biodistribution of DiR labeled P5 and P50 was assessed in tumor bearing mice using a whole body optical imager (Pearl Impulse, Licor). Mice were inoculated with $1\text{--}2 \times 10^6$ PC3 cells on the right hind leg and after 4–8 weeks, when the tumors were 0.5–1 cm in diameter, the mice were used for experiments ($n=4$ for P50, $n=4$ for P5). Before intravenous administration of the NE, a pre-injection image was taken. Subsequently, the NE was injected (amphiphilic lipid dose of 80 $\mu\text{mole/kg}$) and the mice were imaged at 24 h post-injection, sacrificed and the organs were excised and imaged as well. From the *in vivo* images the pre- and post-injection, signal to background ratio (SBR) was determined for the tumor and as controls also for the opposite left hind leg where no tumor was present. The fluorescence intensity measured from the organs was normalized to the organ weight.

RESULTS

Characterization of Nanoemulsions

NEs with different molar content of PEG-DSPE (5, 10, 30, and 50 mol%) were synthesized. Figure 1a shows a schematic

of the NEs. DLS measurements showed that the different NEs were all around 100 nm in size and had a similar polydispersity index (polydispersity index corresponds to the square of the standard deviation divided by the mean size), Fig. 1b. Furthermore, incubation of the different NEs in 10% FBS at 37°C did not result in significant increases in size for any of the NEs, indicating limited protein adsorption occurring on either of the NE surfaces (Fig. 1c and supplementary material S1).

Cellular Uptake of Nanoemulsions

From z-stacks obtained with CLSM we observed that the majority of cell-associated nanoemulsion was internalized by the PC3 cells, see supplementary material S2. Cellular uptake of NIR664-PEG-DSPE labeled P5, P10, P30, and P50 was quantified using flow cytometry. Figure 2a and b shows representative flow cytometric logarithmic fluorescence histograms. Cellular uptake decreased with increasing PEG surface density. P5 was taken up by $76 \pm 12\%$ and $93 \pm 7\%$ of the PC3 cells after 2 h and 4 h of incubation, respectively (Fig. 2c). P50 was internalized only by $20 \pm 8\%$ of the cells after 2 h exposure and by $34 \pm 14\%$ following 4 h of incubation (Fig. 2c).

The median fluorescence intensity of cells incubated for 2 h with P5 was 4.0 ± 1.0 and in case of P50 it was 2.4 ± 1.1 . After 4 h of incubation, the median fluorescence intensity for P5 increased and reached 5.4 ± 2.3 , whereas for P50 it did not change significantly (Fig. 2d).

Nanoemulsion Intracellular Stability

Intracellular stability of double labeled (rhodamine-PE and NIR664-PEG-DSPE) P5 and P30 was studied using CLSM and colocalization analysis. From visual inspections of images in which the NIR664 (red, Fig. 3a and e) and rhodamine (green, Fig. 3b and f) channels were superimposed (Fig. 3c, d, g and h), only partial colocalization of NIR664 and rhodamine probes can be subjectively identified by the appearance of yellow color. This indicated partial intracellular disintegration of both P5 and P30.

This was confirmed by the quantitative colocalization analysis (Fig. 4). From the ICA plots it can be observed that the majority of the voxels have a positive PDM value indicating dependent fluorescence intensity in the two channels for both P5 and P30 (Fig. 4a, b, e, f). The scatter plots show a cloud with the tendency of a positive correlation between the intensities in the two channels for both P5 and P30 (Fig. 4c and g). The R_r value for P5 was 0.45 ± 0.19 and for P30 0.52 ± 0.22 (Fig. 4d and h). The ICQ values for P5 and P30 NEs were 0.31 ± 0.04 and 0.30 ± 0.05 , respectively (Fig. 4d and h). The M_A , describing which fraction of NIR664-PEG-DSPE colocalized with rhodamine-PE, was 0.60 ± 0.18 for P5 and 0.69 ± 0.18 for P30. The M_B , describing which fraction of

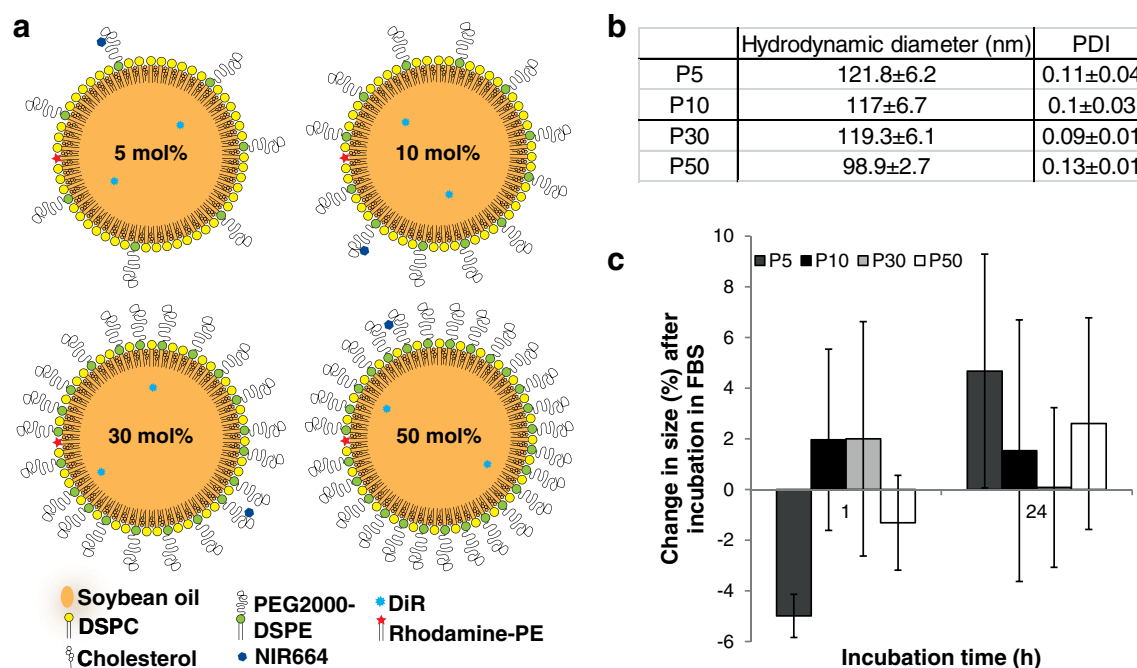


Fig. 1 Nanoemulsion characteristics. **(a):** Cartoons of the nanoemulsions with the 4 different PEG surface densities and the different fluorophores. **(b):** Results from dynamic light scattering size and size distribution measurements. **(c):** The change in size of the nanoemulsions as a function of incubation time in 10% FBS in PBS at 37°C. The data represents the average of 3 measurements and error bars represent \pm standard deviation

rhodamine-PE colocalized with NIR664-PEG-DSPE, was 0.5 ± 0.15 for P5 and 0.46 ± 0.19 for P30 (Fig. 4d and h).

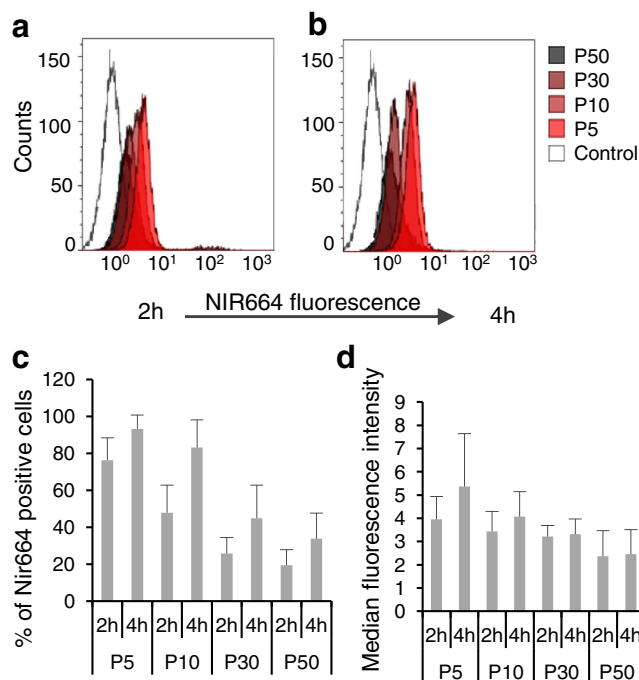


Fig. 2 Cellular uptake of the nanoemulsions as function of PEG surface density. Flow cytometric logarithmic fluorescence histograms of cells incubated with nanoemulsions for 2 h **(a)** and 4 h **(b)**. From the histograms, the percentage of NIR664 positive cells **(c)** and the median fluorescence intensity per cell **(d)** were determined. The data is the average of at least 3 measurements and error bars represent \pm standard deviation.

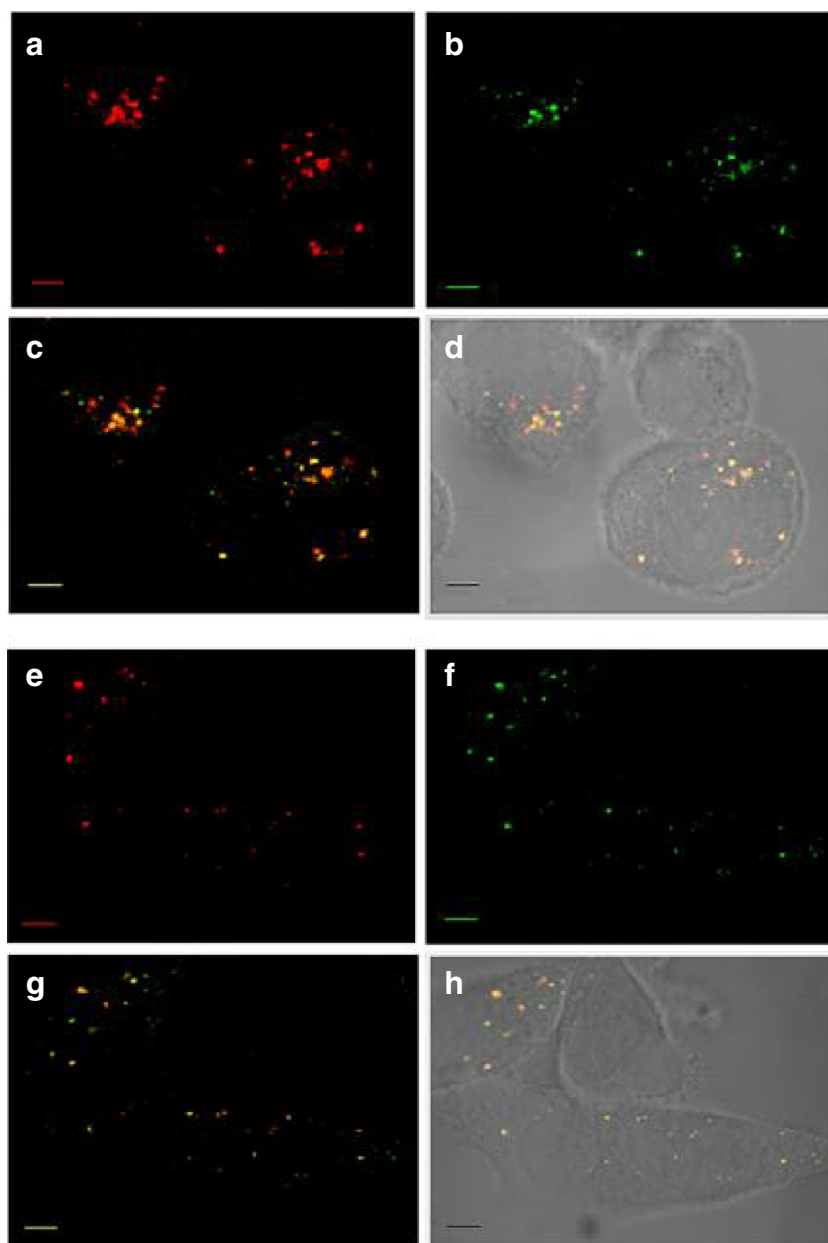
Taken together this colocalization analysis indicates partial intracellular disintegration to a similar extend for both P5 and P30, showing that the PEG surface density did not affect intracellular stability/disintegration of the NEs.

Toxicity and Complement Activation

In the Alamar blue assay it was observed that the viability of PC3 cells incubated with P5, P10, P30, or P50 slightly decreased with increasing NE dose, reaching the lowest viability slightly below 80% at the highest incubation concentrations, see Fig. 5a. However, no significant effects of NE concentration or PEG surface density on cell viability were observed, indicating the NEs are well tolerated by the cells.

In the monocyte assays, no or only very low levels (non-significant; unpaired, two-tailed *t*-test) of cytokines were observed after exposure to P5 or P50. In the first experiment series positive controls for inflammasome activation Leu-Leu-OMe and ATP showed 195.0 ± 39.0 and 470.9 ± 74.6 pg/ml IL-1 β , respectively. In the second experiment series the responses to the positive controls were also normal and no significant increase in concentration of any of the 17 cytokines analyzed with multiplex were observed after exposure to P5 or P50. Also in the whole blood assay, no significant changes in cytokine concentrations were observed after exposure to the NEs. These results are in line with the Alamar blue assay, indicating the NEs are well tolerated by different cell types.

Fig. 3 CLSM images of PC3 cells incubated with either P5 (**a–d**) or P30 (**e–h**). NIR664 fluorescence is shown in red (**a, e**) and rhodamine fluorescence in green (**b, f**). Overlays of the two channels are shown in (**c**) and (**g**). In (**d**) and (**h**) both NIR664 and rhodamine channels are overlain on the corresponding DIC image showing the cells. Scale bars: 5 μ m.



Importantly, in whole blood CD11b expression on granulocytes and the concentration of TCC were increased after exposure to P50, but not after exposure to P5 (Fig. 5b and c). This indicated that P50 activated the complement system, whereas P5 did not.

***In Vivo* Circulation**

The circulation half-lives for DiR labeled P5, P10, P30 and P50 are shown in Fig. 6a. No difference in circulation half-lives for P5 and P10 was observed. P30 circulated shorter than P5 and P10, and P50 had a significantly shorter circulation half-life than P5, P10 and P30. The circulation

half-life decreased from approximately 200 min for P5 to 40 min for P50.

***In Vivo* Biodistribution**

The biodistribution of DiR labeled P5 and P50 was studied in tumor bearing mice using whole body *in vivo* fluorescence imaging and *ex vivo* fluorescence imaging of the excised organs 24 h post-injection. *In vivo*, tumor accumulation of both agents was observed, and seemed more pronounced in case of P50, as indicated by the higher SBR in the tumor (Fig. 6b and e). However, from the images in Fig. 6e it can be observed that P50 was distributed throughout the mouse, whereas P5 was to a large extent confined to the

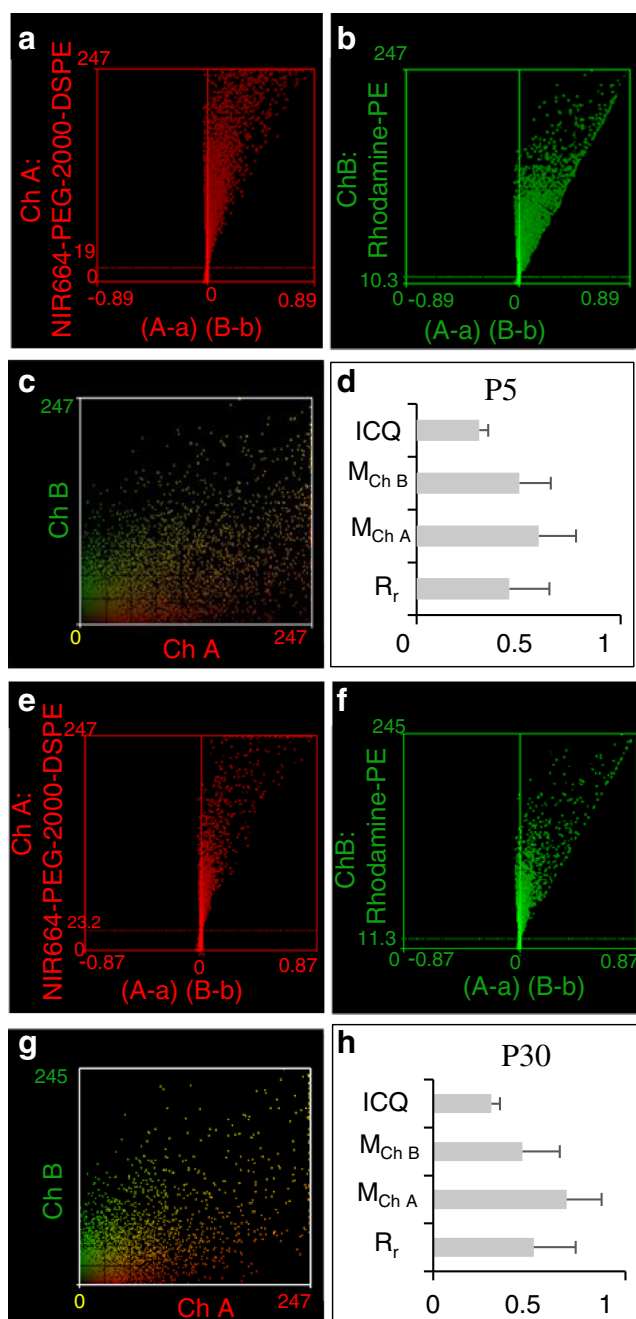


Fig. 4 Results from the colocalization analysis for P5 (**a–d**) and P30 (**e–h**) after 2 h of incubation. The ICA plots shown (**a, b, e, f**) and scatter plots (**c, g**) are obtained from single cells and are representative for the average. Colocalization parameters (**d, h**) were obtained by analysis of z-stacks of 29 cells for both P5 and P30. Error bars represent \pm standard deviation.

organs of the mononuclear phagocyte system (e.g. liver/spleen) and the tumor. Additionally, the SBR of the control leg (containing no tumor) was higher in the mice injected with P50 (Fig. 6b). Combined with the *ex vivo* observation that actual tumor accumulation was very similar for both agents (Fig. 6c, d and f), this indicated that increased PEG surface density does not result in increased accumulation in the tumor.

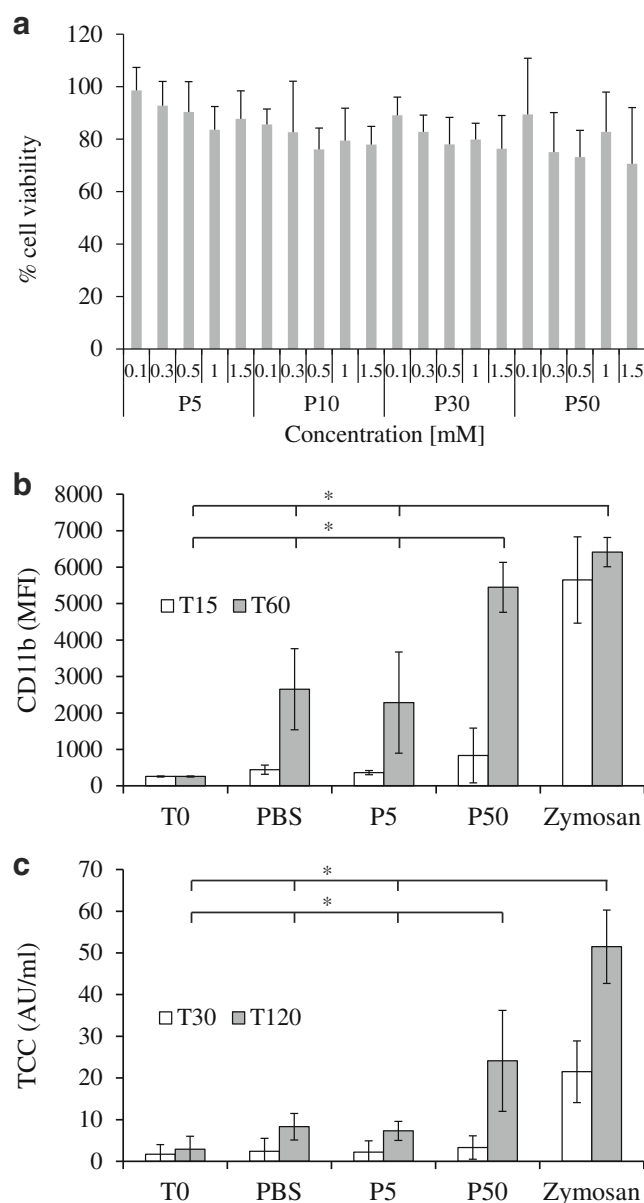


Fig. 5 Cytotoxicity and complement activation. (**a**): Cell viability of PC3 cells in the alamar blue assay after 2 h exposure to P5, P30, or P50. (**b**): Mean amount of CD11b (median fluorescence intensity: MFI) expressed by granulocytes in whole blood ($n=4$) after no (T0), 15 (T15) and 60 (T60) min exposure to P5 or P50. P50 T60 is significantly higher than P5, PBS and T0. Zymosan T60 is significantly higher than P5, PBS and T0. (**c**): Mean concentration of TCC in whole blood ($n=4$) after no (T0), 30 (T30) and 120 (T120) min exposure to P5 or P50. P50 T120 is significantly higher than P5, PBS and T0. Zymosan T120 is significantly higher than P50, P5, PBS and T0. The error bars represent \pm standard deviation. In (**b**) and (**c**) zymosan served as positive and PBS as negative control and * indicates $p < 0.05$ (unpaired, two-tailed t-test).

Furthermore, both P5 and P50 showed highest accumulation in the liver and spleen 24 h after injection in the *ex vivo* organ imaging. Although this was much more pronounced for P5, especially in case of the spleen, this may in part be explained by the much longer circulation residence time of P5 as compared to P50.

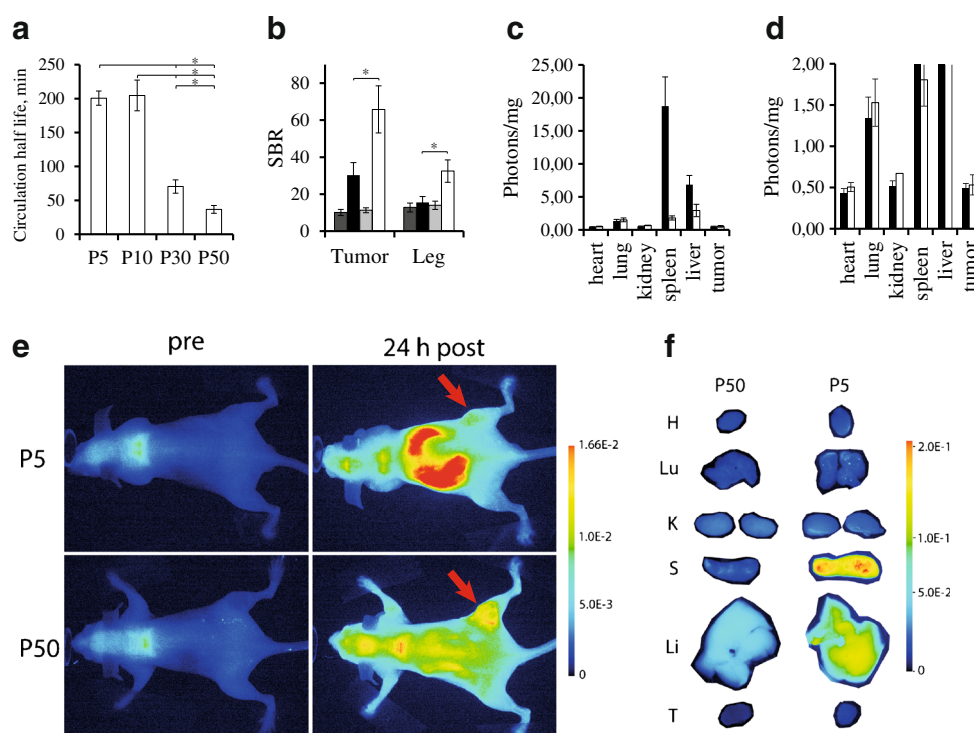


Fig. 6 *In vivo* results. (a): Circulation half-lives of the different formulations ($n=3$ for each). * $p < 0.025$ (unpaired, two-tailed *t*-test) (b): The *in vivo* signal to background ratio (SBR) for the tumor and the control leg. * $p < 0.025$ (unpaired, two-tailed *t*-test) (dark grey: pre-injection P5, black: 24 h post injection P5, light grey: pre-injection P50, white: 24 h post injection P50). (c): The ex vivo photon count per mg of tissue for the tumor and organs (black: P5, white: P50). (d): The same as Fig. 6c, but with different scaling on the y-axis. In (b–d): $n=4$ and in (a–d): error bars represent \pm standard deviation. (e): Pre- and post-injection *in vivo* images of mice injected with P5 or P50. The mouse is facing with the back, and the tumor is present on its right hind leg, indicated by arrows. (f): Ex vivo images of the organs excised at 24 h post injection of the same mice as in (e). In (f) H heart, Lu lungs, K kidneys, S spleen, Li liver, and T tumor.

DISCUSSION

The effect of PEG surface density on several important aspects of the *in vitro* and *in vivo* behavior of NEs was studied. The NE platform we utilized allowed for variation of the PEG surface density in a wide range from 5 to 50 mol%. It was found that increasing PEG surface density resulted in complement activation and reduced *in vivo* circulation half-lives, did not increase intracellular stability and passive tumor targeting and led to an increased accumulation in organs other than the spleen, liver and tumor.

There was a tendency of the nanoparticle size becoming smaller with increasing PEG-DSPE content. In PEG-DSPE, the hydrophilic part is very large in comparison to its double hydrophobic fatty acid tail. Consequently, the curvature of the membrane in which PEG-DSPE is incorporated increases, resulting in a decrease of the NE diameter. Since the size of nanoparticles can affect cellular uptake [30], the diameter of NEs was kept nearly constant by increasing the amount of soybean oil in the core with increasing PEG-DSPE content.

Increasing PEG surface density has been shown to result in decreased non-specific cellular uptake of lipid-based nanoparticles [19,24] and our *in vitro* experiments were in line with this. As protein absorption was very similar for the different NEs

studied, the decrease in cellular uptake may be explained by the more negative zeta potential at the higher PEG surface densities [24]. The cell membrane is slightly negatively charged, hence electrostatic repulsion between the NE and the cell membrane increases with increasing PEG surface density.

Cellular internalization of intact nanoparticles is an important aspect of nanoparticle drug delivery [31]. Thus, intracellular nanoparticle stability and drug release play a vital role. Furthermore, PEG-DSPE is known to sterically stabilize lipid-based nanoparticles in aqueous dispersion [14,18]. However, to the best of our knowledge, no work on intracellular stability of lipid-based nanoparticles as a function of PEG surface density has been published. For these reasons we studied the intracellular stability of the NE as a function of PEG surface density. Our colocalization study of double labeled P5 and P30 showed that the intracellular stability is not affected by PEG-surface density. This indicates that once internalized, the NE PEG surface density does not affect NE stability/disintegration. As such, varying the PEG surface density does not seem to be a tool allowing for tuning of drug release profiles in a potential therapeutic application.

In vivo, we observed a remarkable decrease in circulation half-life with increased NE PEG-DSPE content. Others have

observed that *in vivo* circulation times of liposomes were increasing with PEG2000 surface density up to 5 mol% and for 5 and 10 mol% no difference was observed in case of these liposomes, which is in line with our results for P5 and P10 mol% [22,23]. In another study, the blood concentration 30 min post-injection was similar for NEs containing 12 and 35 mol% PEG-PE [18]. This deviates from our observations, which may be due to the other amphiphiles and oil used or due to the fact that we assessed circulation times over 24 h and Liu *et al.* measured blood concentrations 30 min after injection [18].

The complement receptor CD11b was found to be up-regulated on granulocytes after exposure to P50, but not after exposure to P5. CD11b generally binds to complement opsonins and facilitates phagocytosis, hence plasma clearance of opsonized substances. As such, our observations provide a strong indication that complement activation resulted in enhanced plasma clearance and explain the decreased circulation times for the NEs with higher PEG surface density.

PEGylation of nanoparticles generally reduces immunogenic potency by masking potential antigen binding sites on the nanoparticle surface [32,33]. Therefore it could be expected that P5 would adsorb more proteins when exposed to FBS and produce more pronounced complement activation than P50 in this study. However, observed protein adsorption during incubation in 10% FBS was minimal for all NEs studied and complement activation was only observed in case of P50 and not in case of P5.

Interestingly, in accordance with our observations, complement activation has been reported to increase with increasing PEG concentration [34]. Moreover, it has been established that PEG [34,35] and the anionic PEG-phospholipid conjugates [36,37] can activate the complement system under certain conditions. Reduced PEG-chain mobility, as is the case for increased PEG surface density, has also been proposed to allow for more permanent binding of opsonins and as such increased complement activation [38]. Although these observations are in line with our findings, the exact molecular mechanisms playing a role in complement activation by PEGylated nanoparticles remain elusive [39].

Despite the difference in circulation times, no clear differences were observed in tumor accumulation at 24 h post-injection. In case of P5, 24 h represents 7.2 circulation half-lives, whereas in case of P50 it represents 36 circulation half-lives, which may indicate that at earlier time points post-injection accumulation of P50 may have been higher than P5. However, P50 was observed to accumulate nonspecifically throughout the mouse to a much higher degree than P5 at 24 h post injection. Therefore, also for a favorable biodistribution and tumor specificity, relatively low PEG-DSPE content is most suitable.

CONCLUSION

In conclusion, we have prepared NEs with diameters of approximately 100 nm with the level of PEG surface density varying from 5 to 50 mol%. The NEs were found not to be cytotoxic, which is important for *in vivo* applications. To the best of our knowledge the current study is the first to investigate the effect of PEG surface density on the intracellular stability of lipid-based nanoparticles. An important novel finding was that intracellular stability of nanoemulsions is unaffected by PEG surface density. Unexpectedly, *in vivo* circulation half-lives decreased with increasing PEG surface density. A plausible explanation is the observed complement activation by NE with high PEG-DSPE content, but not by NE with low PEG-DSPE content. The biodistribution and tumor accumulation of P5 and P50 in tumor bearing mice was similar, however, P50 was found to accumulate throughout the mice, whereas P5 was to a large extent confined to the organs of the mononuclear phagocyte system and the tumor. Taken together, this demonstrates that the optimal PEG-DSPE content of lipid-based drug delivery systems for tumor targeting is below 10 mol%.

ACKNOWLEDGMENTS AND DISCLOSURES

We gratefully thank K. Grendstad Sæterbø for help with cell culturing and S. Eggen for help with the xenografts. The work was supported by the Norwegian Cancer Society, Medical Imaging Laboratory (MI-Lab, NTNU, Norway), and the Slovak Research and Development Agency under the contract LPP-0250-09.

REFERENCES

1. Duivenvoorden R, Tang J, Cormode DP, Mieszawska AJ, Izquierdo-Garcia D, Ozcan C, *et al.* A statin-loaded reconstituted high-density lipoprotein nanoparticle inhibits atherosclerotic plaque inflammation. *Nat Commun.* 2014;5:3065.
2. Quan L, Zhang Y, Crielard BJ, Dusad A, Lele SM, Rijcken CJ, *et al.* Nanomedicines for inflammatory arthritis: head-to-head comparison of glucocorticoid-containing polymers, micelles, and liposomes. *ACS Nano.* 2014;8(1):458–66.
3. Gillies RJ, Schornack PA, Secomb TW, Raghunand N. Causes and effects of heterogeneous perfusion in tumors. *Neoplasia.* 1999;1(3): 197–207.
4. Less JR, Skalak TC, Sevic EM, Jain RK. Microvascular architecture in a mammary carcinoma: branching patterns and vessel dimensions. *Cancer Res.* 1991;51(1):265–73.
5. Matsumura Y, Maeda H. A new concept for macromolecular therapeutics in cancer chemotherapy: mechanism of tumoritropic accumulation of proteins and the antitumor agent smancs. *Cancer Res.* 1986;46(12 Pt 1):6387–92.
6. Seymour LW. Passive tumor targeting of soluble macromolecules and drug conjugates. *Crit Rev Ther Drug Carrier Syst.* 1992;9(2): 135–87.

7. Prabhakar U, Maeda H, Jain RK, Sevick-Muraca EM, Zamboni W, Farokhzad OC, *et al.* Challenges and key considerations of the enhanced permeability and retention effect for nanomedicine drug delivery in oncology. *Cancer Res.* 2013;73(8):2412–7.
8. Wagner V, Dullaart A, Bock AK, Zweck A. The emerging nanomedicine landscape. *Nat Biotechnol.* 2006;24(10):1211–7.
9. Gianella A, Jarzyna PA, Mani V, Ramachandran S, Calcagno C, Tang J, *et al.* Multifunctional nanoemulsion platform for imaging guided therapy evaluated in experimental cancer. *ACS Nano.* 2011;5(6):4422–33.
10. Lanza GM, Winter PM, Caruthers SD, Hughes MS, Hu G, Schmieder AH, *et al.* Theragnostics for tumor and plaque angiogenesis with perfluorocarbon nanoemulsions. *Angiogenesis.* 2010;13(2):189–202.
11. Chan JM, Zhang L, Yuet KP, Liao G, Rhee JW, Langer R, *et al.* PLGA-lecithin-PEG core-shell nanoparticles for controlled drug delivery. *Biomaterials.* 2009;30(8):1627–34.
12. Cormode DP, Skajaa GO, Delshad A, Parker N, Jarzyna PA, Calcagno C, *et al.* A versatile and tunable coating strategy allows control of nanocrystal delivery to cell types in the liver. *Bioconjug Chem.* 2011;22(3):353–61.
13. Dubertret B, Skourides P, Norris DJ, Noireaux V, Brivanlou AH, Libchaber A. In vivo imaging of quantum dots encapsulated in phospholipid micelles. *Science.* 2002;298(5599):1759–62.
14. Allen TM. Long-circulating (sterically stabilized) liposomes for targeted drug delivery. *Trends Pharmacol Sci.* 1994;15(7):215–20.
15. Howard MD, Jay M, Dziubla TD, Lu X. PEGylation of nanocarrier drug delivery systems: state of the Art. *J Biomed Nanotechnol.* 2008;4(2):133–48.
16. Papahadjopoulos D, Allen TM, Gabizon A, Mayhew E, Matthey K, Huang SK, *et al.* Sterically stabilized liposomes: improvements in pharmacokinetics and antitumor therapeutic efficacy. *Proc Natl Acad Sci U S A.* 1991;88(24):11460–4.
17. Ryan SM, Mantovani G, Wang X, Haddleton DM, Brayden DJ. Advances in PEGylation of important biotech molecules: delivery aspects. *Expert Opin Drug Deliv.* 2008;5(4):371–83.
18. Liu F, Liu D. Long-circulating emulsions (oil-in-water) as carriers for lipophilic drugs. *Pharm Res.* 1995;12(7):1060–4.
19. Allen TM, Austin GA, Chonn A, Lin L, Lee KC. Uptake of liposomes by cultured mouse bone marrow macrophages: influence of liposome composition and size. *Biochim Biophys Acta (BBA) - Biomembr.* 1991;1061(1):56–64.
20. Klibanov AL, Maruyama K, Torchilin VP, Huang L. Amphipathic polyethyleneglycols effectively prolong the circulation time of liposomes. *FEBS Lett.* 1990;268(1):235–7.
21. Wu NZ, Da D, Rudoll TL, Needham D, Whorton AR, Dewhirst MW. Increased microvascular permeability contributes to preferential accumulation of Stealth liposomes in tumor tissue. *Cancer Res.* 1993;53(16):3765–70.
22. Dos Santos N, Allen C, Doppin A-M, Anantha M, Cox KAK, Gallagher RC, *et al.* Influence of poly(ethylene glycol) grafting density and polymer length on liposomes: Relating plasma circulation lifetimes to protein binding. *Biochim Biophys Acta (BBA) - Biomembr.* 2007;1768(6):1367–77.
23. Schifflers RM, Bakker-Woudenberg IAJM, Snijders SV, Storm G. Localization of sterically stabilized liposomes in *Klebsiella pneumoniae*-infected rat lung tissue: influence of liposome characteristics. *Biochim Biophys Acta (BBA) - Biomembr.* 1999;1421(2):329–39.
24. Hak S, Helgesen E, Hektoen HH, Huuse EM, Jarzyna PA, Mulder WJ, *et al.* The effect of nanoparticle polyethylene glycol surface density on ligand-directed tumor targeting studied in vivo by dual modality imaging. *ACS Nano.* 2012;6(6):5648–58.
25. Johnsson M, Edwards K. Liposomes, disks, and spherical micelles: aggregate structure in mixtures of gel phase phosphatidylcholines and poly(ethylene glycol)-phospholipids. *Biophys J.* 2003;85(6):3839–47.
26. Jarzyna PA, Skajaa T, Gianella A, Cormode DP, Samber DD, Dickson SD, *et al.* Iron oxide core oil-in-water emulsions as a multifunctional nanoparticle platform for tumor targeting and imaging. *Biomaterials.* 2009;30(36):6947–54.
27. Bolte S, Cordelieres FP. A guided tour into subcellular colocalization analysis in light microscopy. *J Microsc.* 2006;224(Pt 3):213–32.
28. Boyum A. Separation of leukocytes from blood and bone marrow. *Scand J Clin Lab Invest.* 1968;21 Suppl 97:7.
29. Mollnes TE, Brekke OL, Fung M, Fure H, Christiansen D, Bergseth G, *et al.* Essential role of the C5a receptor in *E. coli*-induced oxidative burst and phagocytosis revealed by a novel lepirudin-based human whole blood model of inflammation. *Blood.* 2002;100(5):1869–77.
30. Kulkarni S, Feng S-S. Effects of particle size and surface modification on cellular uptake and biodistribution of polymeric nanoparticles for drug delivery. *Pharm Res.* 2013;1–11.
31. Drummond DC, Noble CO, Hayes ME, Park JW, Kirpotin DB. Pharmacokinetics and in vivo drug release rates in liposomal nanocarrier development. *J Pharm Sci.* 2008;97(11):4696–740.
32. Faraji AH, Wipf P. Nanoparticles in cellular drug delivery. *Bioorg Med Chem.* 2009;17(8):2950–62.
33. Harris JM, Martin NE, Modi M. Pegylation: a novel process for modifying pharmacokinetics. *Clin Pharmacokinet.* 2001;40(7):539–51.
34. Hamad I, Hunter AC, Szebeni J, Moghimi SM. Poly(ethylene glycol)s generate complement activation products in human serum through increased alternative pathway turnover and a MASP-2-dependent process. *Mol Immunol.* 2008;46(2):225–32.
35. Szebeni J. Complement activation-related pseudoallergy: a new class of drug-induced acute immune toxicity. *Toxicology.* 2005;216(2–3):106–21.
36. Garbuzenko O, Zalipsky S, Qazen M, Barenholz Y. Electrostatics of PEGylated micelles and liposomes containing charged and neutral lipopolymers. *Langmuir : ACS J Surf Colloids.* 2005;21(6):2560–8.
37. Moghimi SM, Hamad I, Andresen TL, Jorgensen K, Szebeni J. Methylation of the phosphate oxygen moiety of phospholipid-methoxy(polyethylene glycol) conjugate prevents PEGylated liposome-mediated complement activation and anaphylatoxin production. *FASEB J.* 2006;20(14):2591–3.
38. Blume G, Cevc G. Molecular mechanism of the lipid vesicle longevity in vivo. *Biochim Biophys Acta.* 1993;1146(2):157–68.
39. Moghimi SM, Andersen AJ, Hashemi SH, Lettierio B, Ahmadvand D, Hunter AC, *et al.* Complement activation cascade triggered by PEG-PL engineered nanomedicines and carbon nanotubes: the challenges ahead. *J Control Release : Off J Control Release Soc.* 2010;146(2):175–81.